

## Role of initial transverse momentum in a hybrid approach

Niklas Götz <sup>1,2</sup>, Lucas Constantin <sup>1</sup>, and Hannah Elfner <sup>1,2,3,4</sup>

<sup>1</sup>*Goethe University Frankfurt, Department of Physics, Institute for Theoretical Physics, 60438 Frankfurt, Germany*

<sup>2</sup>*Frankfurt Institute for Advanced Studies, 60438 Frankfurt am Main, Germany*

<sup>3</sup>*GSI Helmholtzzentrum für Schwerionenforschung, 64291 Darmstadt, Germany*

<sup>4</sup>*Helmholtz Research Academy Hesse for FAIR (HFHF), GSI Helmholtz Center, Campus Frankfurt, 60438 Frankfurt am Main, Germany*



(Received 17 January 2024; revised 15 April 2024; accepted 14 August 2024; published 3 September 2024)

**Background:** Significant theoretical uncertainties exist with respect to the initial condition of the hydrodynamic description of ultrarelativistic heavy-ion collisions. Several approaches exist, of which some contain initial momentum information. Its impact is commonly assumed to be small and final flow is seen as a linear response to the initial-state eccentricity.

**Purpose:** The purpose of this work is to study the effect of exchanging initial condition models in a modular hybrid approach, especially regarding changes in the event-by-event correlations of elliptic and triangular flow with initial-state quantities like eccentricity and initial-state transverse momentum.

**Method:** This study is performed in the hybrid approach SMASH-vHLL, composed of the hadronic transport approach SMASH and the (3 + 1)d viscous hydrodynamic code vHLL. The initial condition models investigated are SMASH IC, T<sub>R</sub>ENTo, and IP-Glasma. Correlations are calculated on an event-by-event basis between the eccentricities and momentum anisotropies of the initial state as well as the momentum anisotropies in the final state, both for central and off-central collisions for AuAu collisions at  $\sqrt{s_{NN}} = 200$  GeV. The response of the final-state to initial-state properties is studied.

**Results:** This work demonstrates that, although averaged values for the initial eccentricities of these models are very similar, substantial differences exist both in the distributions of eccentricities, the correlations among the initial-state properties as well as in the correlations between initial-state and final-state properties. Notably, whereas initial-state momentum anisotropy is shown to not affect the final-state flow, the presence of radial flow affects the emergence of final-state momentum anisotropies.

**Conclusions:** Inclusion of radial flow in the linear fit improves the prediction of final-state flow from initial-state properties. The presence of transverse momentum in the initial state has an effect on the emergence of flow and is therefore a relevant part of initial-state models, challenging the common understanding of final-state momentum anisotropies being a linear response to initial-state eccentricity only.

DOI: [10.1103/PhysRevC.110.034901](https://doi.org/10.1103/PhysRevC.110.034901)

### I. INTRODUCTION

One of the most important results of studying fundamental properties of matter by colliding atomic nuclei at relativistic velocities is the observation of collective behavior. Gold-gold collisions at the Relativistic Heavy Ion Collider (RHIC) at BNL showed signatures of a strongly interacting system with a small mean free path, as long-range correlations and a significant elliptic flow have been observed [1,2].

The current understanding for this elliptic (as well as higher order) flow is the existence of initial-state eccentricities  $\epsilon_n$ , originating from the geometry of the collision and initial-state fluctuations. They result in pressure anisotropies during the evolution of the hot and dense matter. These, in turn, lead to the momentum of the particles emitted to depend on the azimuthal angle [3]. The resulting flows  $v_n$  are often assumed to be a linear response to the  $\epsilon_n$  [4].

From the theoretical perspective, heavy-ion collisions have been successfully described in hybrid approaches. These are based on relativistic viscous fluid dynamics for the hot and

dense stage and hadronic transport for the nonequilibrium rescattering [5–11]. They combine the successful description of hadronic transport at low energies, where hadronic interactions prevail, with the high energy description of relativistic hydrodynamic calculations. The hadronic transport typically serves as a hadronic afterburner, which has shown to successfully reproduce experimental observables [12].

Relativistic viscous hydrodynamic calculations provide direct access to the properties of the medium and a potential phase transition, as the equation of state and the transport coefficients are given as an input. Determining the functional form of the shear viscosity over entropy ratio of nuclear matter  $\eta/s$  is of special interest, as one expects a minimum near the point of phase transition [13–20]. As the shear viscosity counteracts pressure gradients in the fluid during hydrodynamic evolution, its main effect is the reduction of the flow coefficients. Therefore, the flow coefficients are the main observables to study  $\eta/s$  [3]. In order to determine the minimum of the shear viscosity as a function of the temperature, one commonly resorts to Bayesian inference, which optimizes the

input parameters, including the ones for the parametrization of the shear viscosity, in order to describe experimental data [13,16,17,21,22]. Although this approach has been successful, it also became evident that such an inference is highly model dependent, as has been demonstrated for the choice of the particlization scheme [22].

A similar impact can be expected for choosing different initial condition models. Due to the extremely short lifetime, the initial state of heavy-ion collisions is experimentally not accessible, leading to a variety of initial-state models to exist [5,7,23–36]. This theoretical uncertainty of the initial-state model is potentially limiting the predictive strength of a Bayesian inference based on a singular initial-state model. Indeed, the initial-state model provides the geometry and fluctuations which are evolved into momentum anisotropy in the final state, from which the shear viscosity is primarily extracted [37,38].

In this work, the effect of changing the initial-state model in a hybrid approach is studied. We compare three initial conditions models for Au-Au collisions at  $\sqrt{s_{NN}} = 200$  GeV: the SMASH IC, which performs hadronic interactions until a constant hypersurface of proper time, the parametric model  $T_{R}ENTo$  [34], and the color-glass-condensate-based model IP-Glasma [32]. A special focus is given to event-by-event correlations between initial-state properties and final-state flow observables, as well as to the impact of momentum space in the initial state.

This work is structured as follows: In Sec. II, the hybrid approach SMASH-vHLLC-hybrid, within which this study is performed, is briefly summarized, as well as the different initial conditions used in this study. In Sec. III, we show that, although averaged properties of the initial conditions are similar, systematic differences arise on an event-by-event bases in the correlations between the initial-state and final-state properties. To conclude, a brief summary and outlook can be found in Sec. IV.

## II. MODEL DESCRIPTION

The theoretical calculations presented in this work are performed using the SMASH-vHLLC-hybrid approach [39], which is publicly available and suited for the theoretical description of heavy-ion collisions between  $\sqrt{s_{NN}} = 4.3$  GeV and  $\sqrt{s_{NN}} = 5.02$  TeV. SMASH-vHLLC-hybrid has been shown to reproduce experimental data well across a wide range of collision energies and conserves all charges ( $B$ ,  $Q$ ,  $S$ ). It is especially successful in reproducing the longitudinal baryon dynamics at intermediate collision energies [5], which was the primary motivation behind its development.

In the following section, a short overview of its components is given (a more detailed description can be found in Ref. [5]).

### A. Hybrid approach

Hybrid approaches combine well-established models for the different stages of a heavy-ion collision. The hot and dense stage has been successfully described by (viscous) fluid dynamics. On the other hand, microscopic nonequilibrium

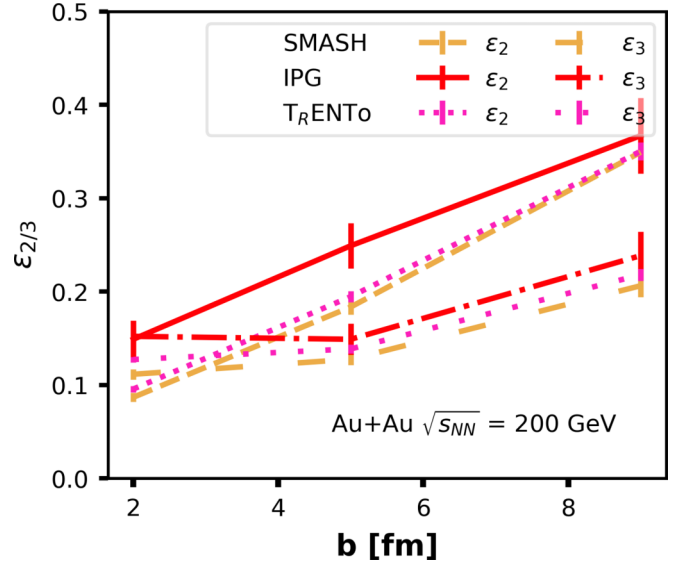


FIG. 1. Initial-state eccentricities for Au-Au collisions at  $\sqrt{s_{NN}} = 200$  GeV as a function of the impact parameter for the three models.

transport approaches are commonly chosen to describe the cold and dilute stage.

### 1. Hydrodynamic evolution

vHLLC [40] is a 3 + 1-Dimensional viscous hydrodynamics code and used to model the evolution of the hot and dense fireball. It solves the hydrodynamic equations

$$\partial_\nu T^{\mu\nu} = 0, \quad (1)$$

$$\partial_\nu J_B^\nu = 0 \quad \partial_\nu J_Q^\nu = 0 \quad \partial_\nu J_S^\nu = 0. \quad (2)$$

These equations represent the conservation of net-baryon, net-charge, and net-strangeness number currents as well as

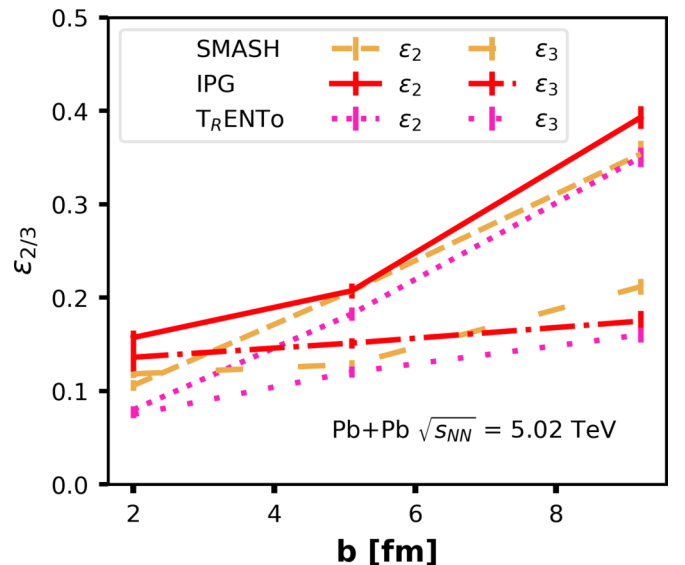


FIG. 2. Initial-state eccentricities for Pb-Pb collisions at  $\sqrt{s_{NN}} = 5.02$  GeV as a function of the impact parameter for the three models.

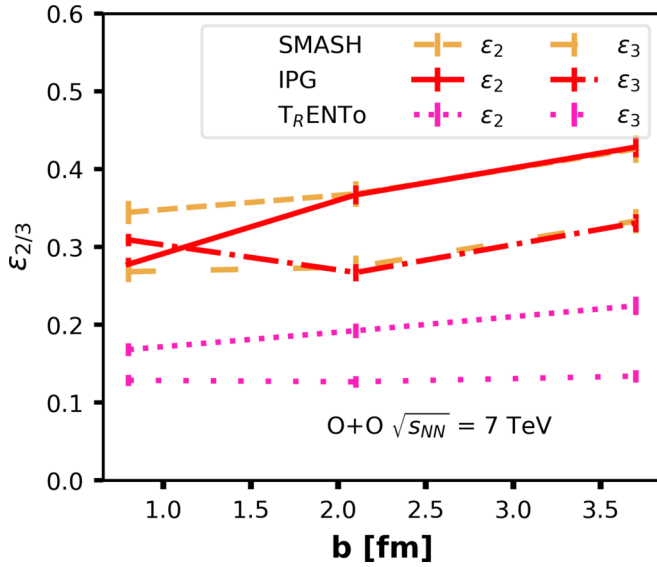


FIG. 3. Initial-state eccentricities for O-O collisions at  $\sqrt{s_{NN}} = 7$  TeV as a function of the impact parameter for the three models.

the conservation of energy and momentum. The energy-momentum tensor is decomposed as

$$T^{\mu\nu} = \epsilon u^\mu u^\nu - \Delta^{\mu\nu}(p + \Pi) + \pi^{\mu\nu} \quad (3)$$

with  $\epsilon$  the local rest frame energy density,  $p$  and  $\Pi$  the equilibrium and bulk pressure and  $\pi^{\mu\nu}$  is the shear stress tensor. These equations are solved in the second order Israel-Stewart framework [41,42].

At this step, particles have been converted into fluid elements which are evolved using a chiral mean-field model equation of state [43–45] which is matched to a hadron resonance gas at low-energy densities. Although the equation of state originates from the parity doublet model, it has

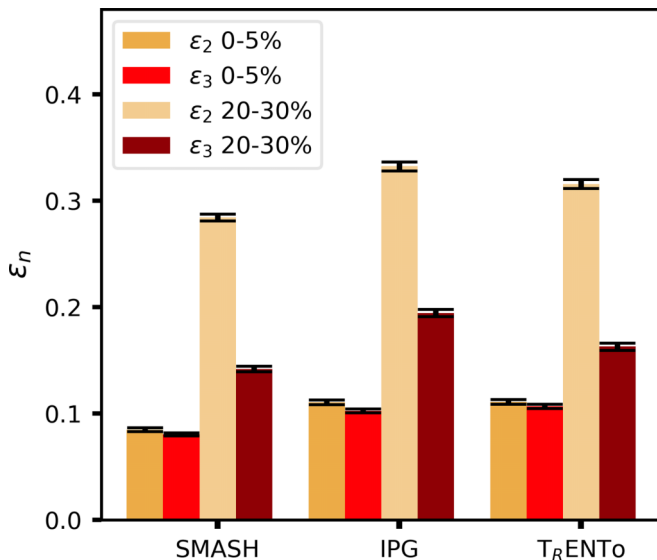


FIG. 4. Initial-state eccentricities for all three models for Au-Au collisions at  $\sqrt{s_{NN}} = 200$  GeV.

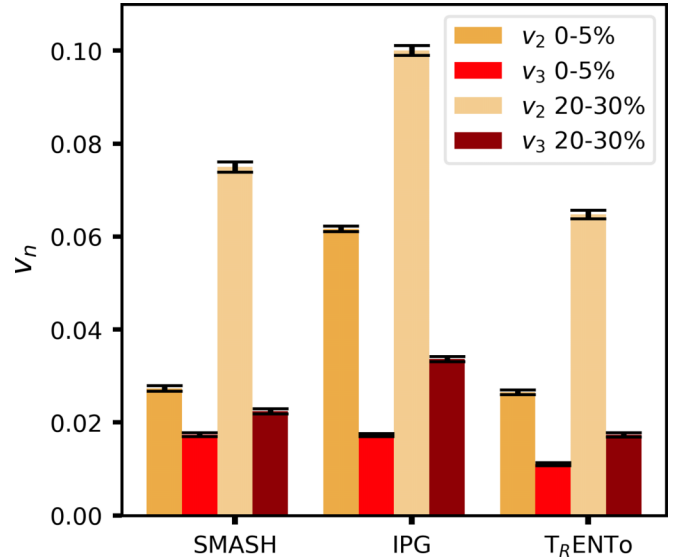


FIG. 5. Final-state flows for all three models for Au-Au collisions at  $\sqrt{s_{NN}} = 200$  GeV.

been shown to match predictions by lattice QCD well. The evolution is performed until a switching energy density is reached, which is set in this work to a default value of  $\epsilon_{\text{switch}} = 0.5$  GeV/fm<sup>3</sup>. At this point, the freeze-out hypersurface is constructed using the CORNELIUS subroutine [46] and the thermodynamical properties of the freeze-out elements are calculated according to the SMASH hadron resonance gas equation of state [5] to prevent discontinuities. The shear viscosity is chosen according to Ref. [47], which defines an energy-density-dependent value of the shear viscosity. This reduces the impact of the choice of the technical parameter  $\epsilon_{\text{sw}}$ , the value energy density at which the degrees of freedom in the description are changed to particles. As the hybrid

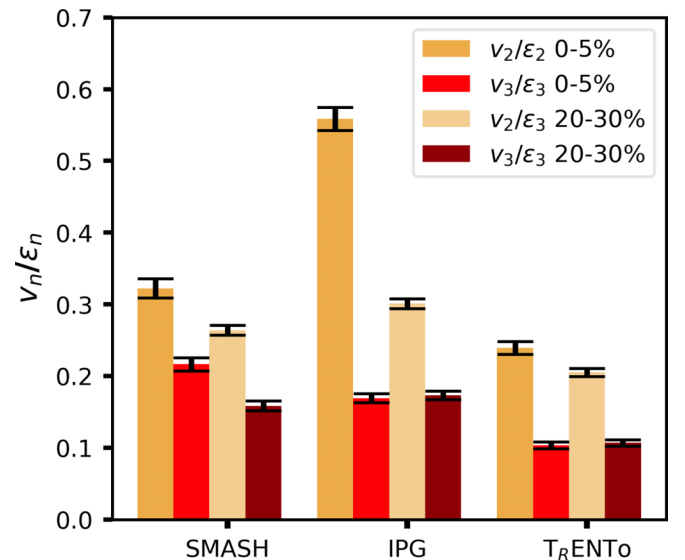


FIG. 6. The response function  $v_n/\epsilon_n$  for all three models for Au-Au collisions at  $\sqrt{s_{NN}} = 200$  GeV.

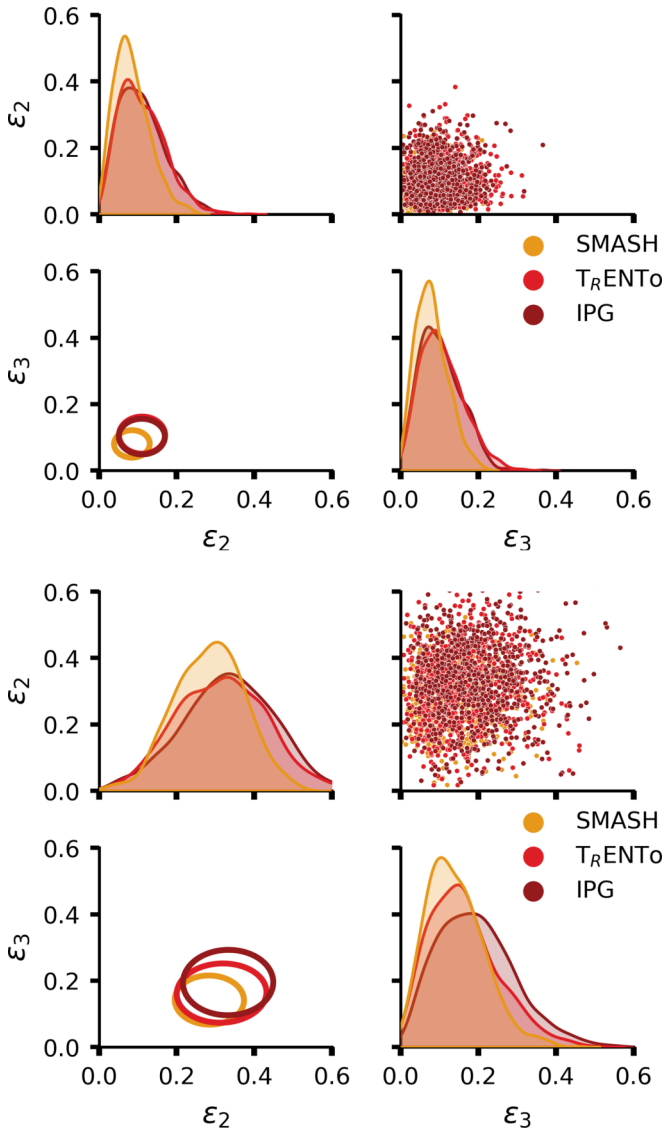


FIG. 7. Distribution of the initial-state eccentricities. On the diagonal, the normalized probability density distribution is shown. On the top right, a 2D scatter plot of the  $\epsilon_2$ - $\epsilon_3$  distribution. The lower left plot shows the relationship of the two quantities, with the center of the ellipse at the mean of  $\epsilon_2$  and  $\epsilon_3$ , width and height are the variance of  $\epsilon_2$  and  $\epsilon_3$ , respectively, and the angle shows the covariance. Data at 0–5% centrality (top) and 20–30% centrality (bottom) for Au-Au collisions at  $\sqrt{s_{NN}} = 200$  GeV.

approach is three dimensional (3D), the 2D initial-state models need to be extended. This is performed in the same way as in Ref. [48]: The 2D profile is extended on a rapidity plateau, until it falls off with a Gaussian profile. For IC models which do not contain inherent information about the available energy in the collision, such as T<sub>R</sub>ENTo and IP-Glasma, the energy profile is rescaled such that the total energy in the system is equal to the energy of all participants. Similarly to Ref. [48], although both T<sub>R</sub>ENTo and IP-Glasma do not contain electric and baryon charge, we deposit both of them in gaussians around the beam rapidity.

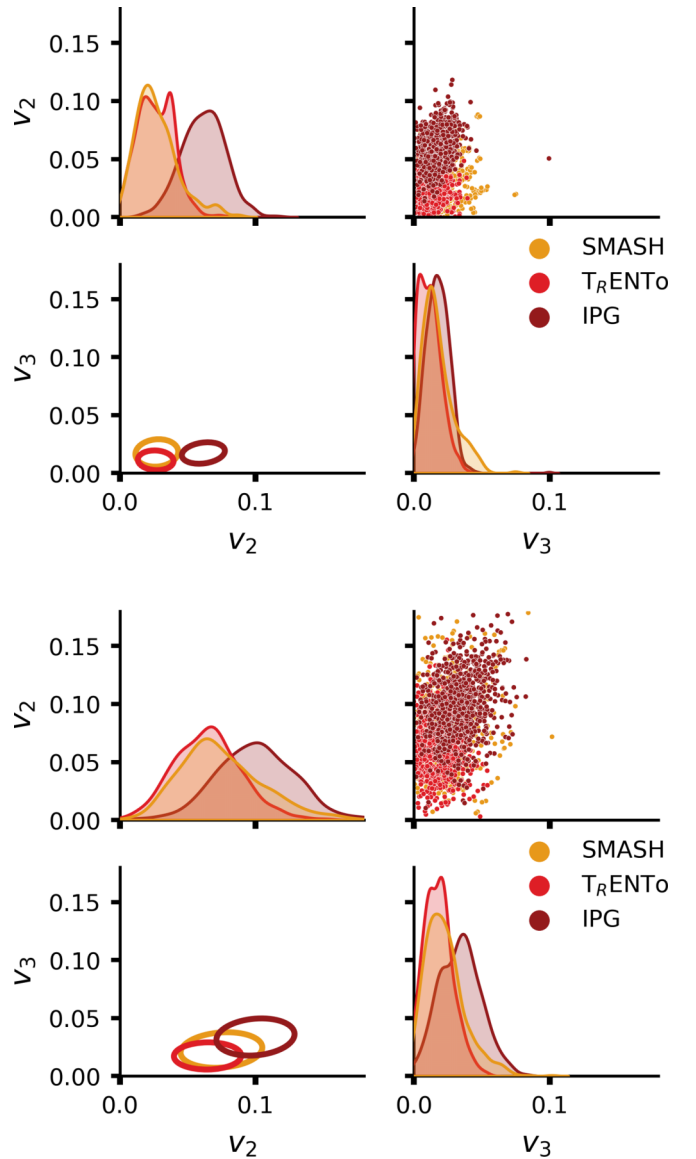


FIG. 8. Distribution of the final-state flows. The diagonal shows the normalized probability density distribution. On the top right, a 2D scatter plot of the  $v_2$ - $v_3$  distribution. The lower left plot shows the relationship of the two quantities, with the center of the ellipse at the mean of  $v_2$  and  $v_3$ , width and height are the variance of  $v_2$  and  $v_3$ , respectively, and the angle shows the covariance. Data at 0–5% centrality (top) and 20–30% centrality (bottom) for Au-Au collisions at  $\sqrt{s_{NN}} = 200$  GeV.

## 2. Particle sampler

As SMASH evolves particles and not fluid elements, particleization has to be performed, for which the SMASH-vHLLC hybrid approach applies the SMASH-hadron-sampler [49]. The SMASH-hadron-sampler employs the grand-canonical ensemble in order to particlize each surface element independently. Hadrons are sampled according to a Poisson distribution with the mean at the thermal multiplicity, and momenta are sampled according to the Cooper-Frye formula [50]. The corrections to the distribution function  $\delta f_{\text{shear}}$

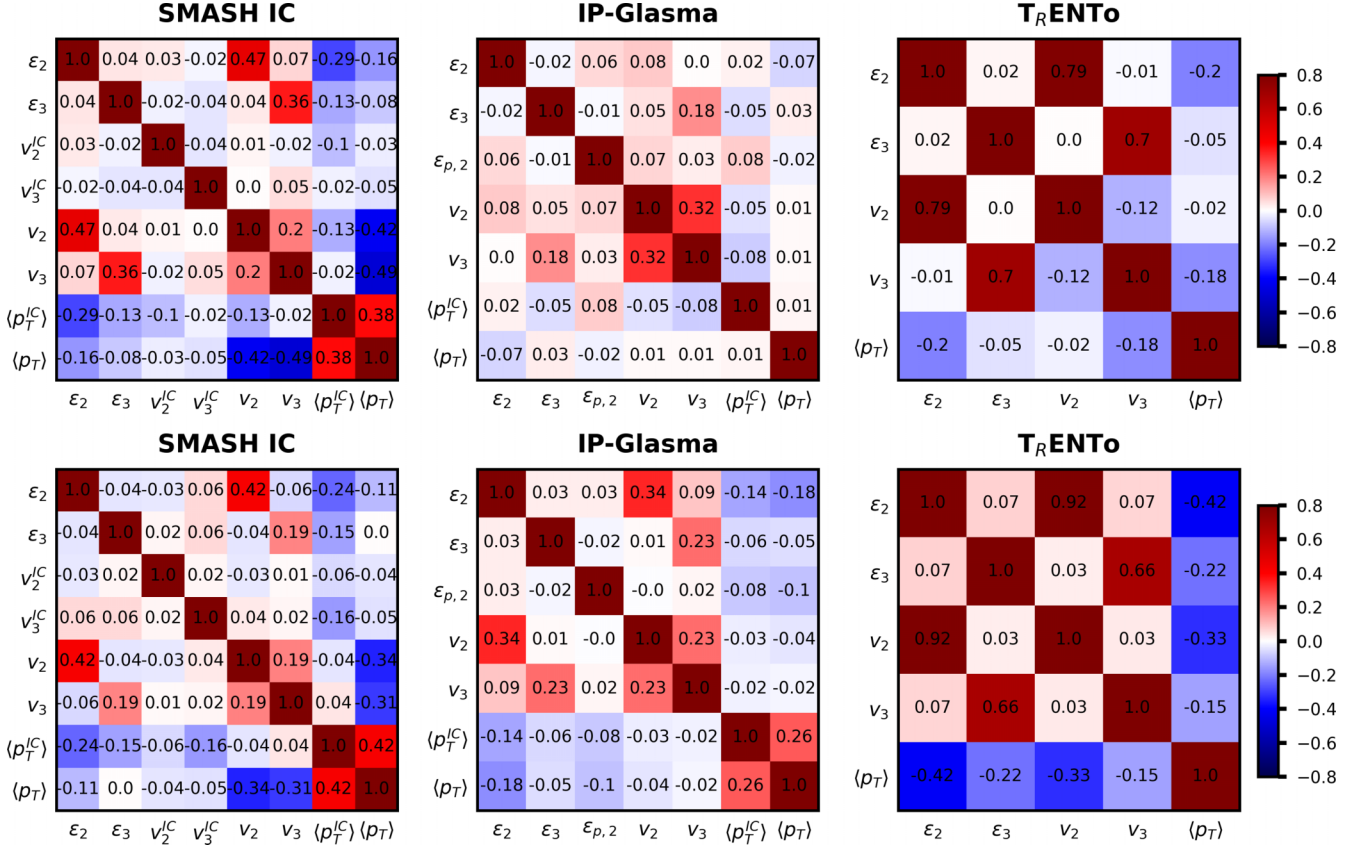


FIG. 9. Pearson correlation matrix for all three initial-state models, at 0–5% centrality (top) and 20–30% centrality (bottom) for Au-Au collisions at  $\sqrt{s_{NN}} = 200$  GeV.

associated to a finite shear viscosity are considered using the Grad’s 14-moment ansatz, for which we assume that the correction is the same for all hadron species, and omit corrections for charge diffusion. Due to  $(T, \mu_B)$  dependence of the shear viscosity, the corrections also have this dependence implicitly. This procedure provides a particle list that can be evolved by SMASH. A more thorough introduction into the sampling procedure can be found in Ref. [6].

### 3. Hadronic transport

SMASH [51–53] effectively solves the relativistic Boltzmann equation by simulating the collision integral through formations, decays and scatterings of hadronic resonances, for which all hadrons listed by the PDG up to a mass of 2.35 GeV are included [54]. For hadronic interactions at high energies, hard scatterings are carried out within Pythia 8 [55] and a soft string model is employed.

The relativistic Boltzmann equation becomes applicable in the late stage of the evolution, when the system has cooled down and expanded far enough to be out of equilibrium. In this last stage of the hybrid evolution, SMASH is employed for hadron rescattering. The hadrons obtained from particlization on the Cooper-Frye hypersurface are propagated back to the earliest time and appear subsequently in the hadronic transport evolution and scatter or decay. The calculation is

terminated when the medium becomes sufficiently dilute for any interactions to cease.

## B. Initial conditions

The input to the viscous relativistic hydrodynamic model is the initial condition, which describes the evolution of the system before the applicability of hydrodynamics. In the following, three different initial condition models are introduced: initial conditions extracted from SMASH, the T<sub>R</sub>ENTo [34] as well as the IP-Glasma [32] model, whereas the SMASH initial condition is the default choice in SMASH-vHLLC-hybrid, both T<sub>R</sub>ENTo as well as IP-Glasma are among the most common choices of initial conditions for Bayesian inference. As T<sub>R</sub>ENTo and IP-Glasma are 2D models, they are suited for high-energy collisions only, whereas SMASH provides full 3D initial conditions. We restrict ourselves therefore to high energies, with a focus on  $\sqrt{s_{NN}} = 200$  GeV. Additionally, we compare our results with SMASH to the intermediate-energy case of  $\sqrt{s_{NN}} = 17.3$  GeV. All three initial condition models sample the original nucleon positions from a Woods-Saxon distribution with identical parameters. Substantial differences arise therefore on the treatment of the collision itself.

### 1. SMASH IC

SMASH generates initial conditions by letting the particles of the colliding nuclei interact until the individual particles

TABLE I. Regression results for  $v_2$  with SMASH IC at 0–5% centrality,  $\sqrt{s_{NN}} = 200$  GeV.

Coefficient	$p$ value	Coefficient	$p$ value	Coefficient	$p$ value	Coefficient	$p$ value	Coefficient	$p$ value	
$\epsilon_2$	$\epsilon_2$	$\epsilon_3$	$\epsilon_3$	$\langle p_T^{\text{IC}} \rangle$	$\langle p_T^{\text{IC}} \rangle$	$v_2^{\text{IC}}$	$v_2^{\text{IC}}$	$v_3^{\text{IC}}$	$v_3^{\text{IC}}$	$r^2$
$2.86 \times 10^{-1} \pm 5.8 \times 10^{-3}$	<b>0.00</b>	–	–	–	–	–	–	–	–	0.763
$2.26 \times 10^{-1} \pm 9.1 \times 10^{-3}$	<b>0.00</b>	$8.09 \times 10^{-2} \pm 9.7 \times 10^{-3}$	<b>0.00</b>	–	–	–	–	–	–	0.783
$1.72 \times 10^{-1} \pm 1.1 \times 10^{-2}$	<b>0.00</b>	–	–	$3.65 \times 10^{-6} \pm 2.9 \times 10^{-7}$	<b>0.00</b>	–	–	–	–	0.804
$2.29 \times 10^{-1} \pm 9.1 \times 10^{-3}$	<b>0.00</b>	–	–	–	–	$4.94 \times 10^{-1} \pm 6.2 \times 10^{-2}$	<b>0.00</b>	–	–	0.781
$1.93 \times 10^{-1} \pm 1.0 \times 10^{-2}$	<b>0.00</b>	$4.50 \times 10^{-2} \pm 1.1 \times 10^{-2}$	<b>0.00</b>	–	–	$2.45 \times 10^{-1} \pm 7.1 \times 10^{-2}$	<b>0.00</b>	$3.14 \times 10^{-1} \pm 7.8 \times 10^{-2}$	<b>0.00</b>	0.794
$1.70 \times 10^{-1} \pm 1.1 \times 10^{-2}$	<b>0.00</b>	$1.12 \times 10^{-2} \pm 1.2 \times 10^{-2}$	$3.57 \times 10^{-1}$	$3.21 \times 10^{-6} \pm 5.3 \times 10^{-7}$	<b>0.00</b>	$2.10 \times 10^{-2} \pm 7.8 \times 10^{-2}$	$7.89 \times 10^{-1}$	$4.77 \times 10^{-2} \pm 8.8 \times 10^{-2}$	$5.87 \times 10^{-1}$	0.804

reach a proper time  $\tau_0$ , on which they are removed from the simulation. This continues until the last particle has reached the hypersurface of constant proper time. This procedure is necessary, as SMASH is realized in Cartesian coordinates, whereas the hydrodynamic evolution is performed in Milne coordinates.  $\tau_0$  corresponds to the passing time of the two nuclei

$$\tau_0 = \frac{R_P + R_T}{\sqrt{\left(\frac{\sqrt{s_{NN}}}{2m_N}\right)^2 - 1}}, \quad (4)$$

where  $R_P$  and  $R_T$  are the radii of projectile and target, respectively.  $\sqrt{s_{NN}}$  is the collision energy and  $m_N$  is the nucleon mass. The passing time is limited to be at least  $0.5 \text{ fm}/c$ , in order to ensure thermalization even for ultrarelativistic collisions. This follows the assumption that at this time local equilibrium is reached and the hydrodynamic description becomes applicable [56,57]. The effect of this is that for fixed center-of-mass energy and nuclei, the passing time is fixed. In order to initialize the hydrodynamic evolution with the iso- $\tau$  particle list generated from SMASH, smoothing has to be performed in order to prevent shock waves. For this purpose, a

Gaussian smearing kernel [6] with the parameters taken from Ref. [5] is applied. The values of the smearing parameters are essential for tuning the initial condition in order to agree with experimental data, as has been shown with similar approaches [58]. It is important to note that the SMASH IC gives access to the initial momentum of the fluid, as well as to charge, baryon, and strange density. Additionally, it has been shown to capture baryon stopping well [5].

## 2. T<sub>R</sub>ENTo

T<sub>R</sub>ENTo is generalized, parametric ansatz for the entropy density deposition from the participant nucleons as follows:

$$T_R(p; T_A, T_B) = (T_A^p + T_B^p)^{\frac{1}{p}}, \quad (5)$$

where  $T_{A,B}$  are the thickness profiles of the two incoming nuclei and  $p$  is a dimensionless parameter which interpolates between the simplified functional forms of the initial entropy density profile in different initial-state models, e.g.,  $p = 1$  corresponds to a Monte Carlo wounded nucleon model, whereas  $p = 0$  is functionally similar to EKRT and IP-Glasma models. Other important parameters are the nucleon width

TABLE II. Regression results for  $v_3$  with SMASH IC at 0–5% centrality,  $\sqrt{s_{NN}} = 200$  GeV.

Coefficient	$p$ value	Coefficient	$p$ value	Coefficient	$p$ value	Coefficient	$p$ value	Coefficient	$p$ value	
$\epsilon_2$	$\epsilon_2$	$\epsilon_3$	$\epsilon_3$	$\langle p_T^{\text{IC}} \rangle$	$\langle p_T^{\text{IC}} \rangle$	$v_2^{\text{IC}}$	$v_2^{\text{IC}}$	$v_3^{\text{IC}}$	$v_3^{\text{IC}}$	$r^2$
–	–	$1.93 \times 10^{-1} \pm 4.7 \times 10^{-3}$	<b>0.00</b>	–	–	–	–	–	–	0.688
$5.28 \times 10^{-2} \pm 7.0 \times 10^{-3}$	<b>0.00</b>	$1.48 \times 10^{-1} \pm 7.5 \times 10^{-3}$	<b>0.00</b>	–	–	–	–	–	–	0.711
–	–	$1.06 \times 10^{-1} \pm 9.4 \times 10^{-3}$	<b>0.00</b>	$2.54 \times 10^{-6} \pm 2.4 \times 10^{-7}$	<b>0.00</b>	–	–	–	–	0.728
–	–	$1.54 \times 10^{-1} \pm 7.5 \times 10^{-3}$	<b>0.00</b>	–	–	$3.11 \times 10^{-1} \pm 4.8 \times 10^{-2}$	<b>0.00</b>	–	–	0.705
$2.98 \times 10^{-2} \pm 7.9 \times 10^{-3}$	<b>0.00</b>	$1.23 \times 10^{-1} \pm 8.5 \times 10^{-3}$	<b>0.00</b>	–	–	$1.09 \times 10^{-1} \pm 5.4 \times 10^{-2}$	$4.50 \times 10^{-2}$	$2.92 \times 10^{-1} \pm 6.0 \times 10^{-2}$	<b>0.00</b>	0.724
$1.66 \times 10^{-2} \pm 8.4 \times 10^{-3}$	$4.75 \times 10^{-2}$	$1.04 \times 10^{-1} \pm 9.4 \times 10^{-3}$	<b>0.00</b>	$1.81 \times 10^{-6} \pm 4.1 \times 10^{-7}$	<b>0.00</b>	$-1.79 \times 10^{-2} \pm 6.1 \times 10^{-2}$	$7.68 \times 10^{-1}$	$1.41 \times 10^{-1} \pm 6.8 \times 10^{-2}$	$3.80 \times 10^{-1}$	0.731

TABLE III. Regression results for  $v_3$  with SMASH IC at 20–30% centrality,  $\sqrt{s_{NN}} = 200$  GeV.

Coefficient	$p$ value	Coefficient	$p$ value	Coefficient	$p$ value	Coefficient	$p$ value	Coefficient	$p$ value	$r^2$
$\epsilon_2$	$\epsilon_2$	$\epsilon_3$	$\epsilon_3$	$\langle p_T^{\text{IC}} \rangle$	$\langle p_T^{\text{IC}} \rangle$	$v_2^{\text{IC}}$	$v_2^{\text{IC}}$	$v_3^{\text{IC}}$	$v_3^{\text{IC}}$	
$2.53 \times 10^{-1} \pm 3.6 \times 10^{-3}$	<b>0.00</b>	–	–	–	–	–	–	–	–	0.869
$2.28 \times 10^{-1} \pm 6.5 \times 10^{-3}$	<b>0.00</b>	$5.51 \times 10^{-2} \pm 1.2 \times 10^{-2}$	<b>0.00</b>	–	–	–	–	–	–	0.872
$1.60 \times 10^{-1} \pm 9.6 \times 10^{-3}$	<b>0.00</b>	–	–	$1.91 \times 10^{-5} \pm 1.9 \times 10^{-6}$	<b>0.00</b>	–	–	–	–	0.885
$2.28 \times 10^{-1} \pm 6.5 \times 10^{-3}$	<b>0.00</b>	–	–	–	–	$4.01 \times 10^{-1} \pm 8.8 \times 10^{-2}$	<b>0.00</b>	–	–	0.872
$2.03 \times 10^{-1} \pm 8.4 \times 10^{-3}$	<b>0.00</b>	$3.37 \times 10^{-2} \pm 1.3 \times 10^{-2}$	<b>0.01</b>	–	–	$2.61 \times 10^{-1} \pm 9.3 \times 10^{-2}$	<b>0.00</b>	$3.30 \times 10^{-1} \pm 1.1 \times 10^{-1}$	<b>0.00</b>	0.876
$1.57 \times 10^{-1} \pm 1.0 \times 10^{-2}$	<b>0.00</b>	$1.31 \times 10^{-3} \pm 1.3 \times 10^{-2}$	$9.20 \times 10^{-1}$	$1.81 \times 10^{-5} \pm 2.3 \times 10^{-6}$	<b>0.00</b>	$-7.09 \times 10^{-3} \pm 9.5 \times 10^{-2}$	$9.41 \times 10^{-1}$	$1.26 \times 10^{-1} \pm 1.1 \times 10^{-1}$	$2.38 \times 10^{-1}$	0.885

and the shape of the nucleon fluctuations. In this work, we use the parameters extracted from Bayesian inference [13], without the use of nuclear substructure. As T<sub>R</sub>ENTo offers only a description of the entropy/energy profile, information about the momentum space is lacking. It can therefore serve as a benchmark in comparison to the other models used in this work, which provide initial momentum information. T<sub>R</sub>ENTo has been extensively used for Bayesian inference studies, as its parametric setup allows to investigate various shapes of the density profile [13,59–61].

### 3. IP-Glasma

Another way to describe the initial state is motivated from the color-glass condensate framework [62], an effective field theory representation of QCD. The CGC action can be written as follows [63]:

$$S_{\text{CGC}} = \int d^4x \left( -\frac{1}{4} F_{\mu\nu}^a F^{a\mu\nu} + J^{a\mu} A_\mu^a \right), \quad (6)$$

where  $J^{a\mu}$  is the source of soft gluons, which is the current represents hard partons, and  $F^{a\mu\nu}$  is the non-Abelian field

strength tensor.  $a$  is the color index. The CGC can be used to generate initial collisions in form of the IP-Glasma model [32,64,65], which uses the IP-Sat approach [24,25] to incorporate the fluctuation of the initial color configuration of the two ultrarelativistic colliding nuclei. The color charges are sources for soft gluon fields at small  $x$ , which, due to their large occupation number, can be treated as classically. This means that their evolution obeys the Yang-Mills equation:

$$[D_\nu, F^{\mu\nu}]^a = J^{a\mu} \quad (7)$$

with  $D_\mu^a = \delta_\mu - igA_\mu t^a$ , where  $t^a$  represents the color SU(3) matrices. The color current  $J^{a\mu} = \delta^{\mu\pm} \rho_{A/B}^a(x^\mp, \mathbf{x}_\perp)$  is generated by nucleus A/B moving along the light-cone direction  $x^+/x^-$  and  $\rho^a$  represents the color charge distribution generated from IP-Sat. The input to fluid dynamics at proper time  $\tau_0$  is generated by solving the classical Yang-Mills equations event by event, which produces the Glasma distributions. The parameters used in this study are the default parameters of the public IP-Glasma repository [66].

 TABLE IV. Regression results for  $v_3$  with SMASH IC at 20–30% centrality,  $\sqrt{s_{NN}} = 200$  GeV.

Coefficient	$p$ value	Coefficient	$p$ value	Coefficient	$p$ value	Coefficient	$p$ value	Coefficient	$p$ value	$r^2$
$\epsilon_2$	$\epsilon_2$	$\epsilon_3$	$\epsilon_3$	$\langle p_T^{\text{IC}} \rangle$	$\langle p_T^{\text{IC}} \rangle$	$v_2^{\text{IC}}$	$v_2^{\text{IC}}$	$v_3^{\text{IC}}$	$v_3^{\text{IC}}$	
–	–	$1.33 \times 10^{-1} \pm 3.8 \times 10^{-3}$	<b>0.00</b>	–	–	–	–	–	–	0.617
$3.76 \times 10^{-2} \pm 3.5 \times 10^{-3}$	<b>0.00</b>	$7.41 \times 10^{-2} \pm 6.6 \times 10^{-3}$	<b>0.00</b>	–	–	–	–	–	–	0.668
–	–	$4.64 \times 10^{-2} \pm 6.9 \times 10^{-3}$	<b>0.00</b>	$1.03 \times 10^{-5} \pm 7.1 \times 10^{-7}$	<b>0.00</b>	–	–	–	–	0.700
–	–	$9.11 \times 10^{-2} \pm 5.9 \times 10^{-3}$	<b>0.00</b>	–	–	$3.85 \times 10^{-1} \pm 4.3 \times 10^{-2}$	<b>0.00</b>	–	–	0.654
$2.31 \times 10^{-2} \pm 4.6 \times 10^{-3}$	<b>0.00</b>	$6.16 \times 10^{-2} \pm 6.9 \times 10^{-3}$	<b>0.00</b>	–	–	$1.79 \times 10^{-1} \pm 5.0 \times 10^{-2}$	<b>0.00</b>	$1.61 \times 10^{-1} \pm 5.8 \times 10^{-2}$	<b>0.01</b>	0.678
$-7.00 \times 10^{-4} \pm 5.4 \times 10^{-3}$	$8.97 \times 10^{-1}$	$4.48 \times 10^{-2} \pm 7.1 \times 10^{-3}$	<b>0.00</b>	$9.44 \times 10^{-6} \pm 1.3 \times 10^{-6}$	<b>0.00</b>	$3.91 \times 10^{-2} \pm 5.2 \times 10^{-2}$	$4.49 \times 10^{-1}$	$5.52 \times 10^{-2} \pm 5.8 \times 10^{-2}$	$3.40 \times 10^{-1}$	0.701

TABLE V. Regression results for  $v_2$  with IP-Glasma at 0–5% centrality,  $\sqrt{s_{NN}} = 200$  GeV.

Coefficient	$p$ value	Coefficient	$p$ value	Coefficient	$p$ value	Coefficient	$p$ value	$r^2$
$\epsilon_2$	$\epsilon_2$	$\epsilon_3$	$\epsilon_3$	$\langle p_T^{\text{IC}} \rangle$	$\langle p_T^{\text{IC}} \rangle$	$\epsilon_p$	$\epsilon_p$	
$4.39 \times 10^{-1} \pm 9.4 \times 10^{-3}$	<b>0.00</b>	–	–	–	–	–	–	0.745
$2.47 \times 10^{-1} \pm 1.2 \times 10^{-2}$	<b>0.00</b>	$2.68 \times 10^{-1} \pm 1.3 \times 10^{-2}$	<b>0.00</b>	–	–	–	–	0.838
$3.55 \times 10^{-2} \pm 1.0 \times 10^{-2}$	<b>0.00</b>	–	–	$5.99 \times 10^{-6} \pm 1.3 \times 10^{-7}$	<b>0.00</b>	–	–	0.930
$2.41 \times 10^{-1} \pm 1.2 \times 10^{-2}$	<b>0.00</b>	–	–	–	–	$4.02 \pm 2.0 \times 10^{-1}$	<b>0.00</b>	0.833
$1.67 \times 10^{-1} \pm 1.2 \times 10^{-2}$	<b>0.00</b>	$1.90 \times 10^{-1} \pm 1.3 \times 10^{-2}$	<b>0.00</b>	–	–	$2.74 \pm 2.0 \times 10^{-1}$	<b>0.00</b>	0.872
$3.36 \times 10^{-2} \pm 1.0 \times 10^{-2}$	<b>0.00</b>	$3.32 \times 10^{-2} \pm 1.1 \times 10^{-2}$	<b>0.00</b>	$5.37 \times 10^{-6} \pm 2.1 \times 10^{-7}$	<b>0.00</b>	$4.07 \times 10^{-1} \pm 1.7 \times 10^{-1}$	$1.73 \times 10^{-2}$	0.931

TABLE VI. Regression results for  $v_3$  with IP-Glasma at 0–5% centrality,  $\sqrt{s_{NN}} = 200$  GeV.

Coefficient	$p$ value	Coefficient	$p$ value	Coefficient	$p$ value	Coefficient	$p$ value	$r^2$
$\epsilon_2$	$\epsilon_2$	$\epsilon_3$	$\epsilon_3$	$\langle p_T^{\text{IC}} \rangle$	$\langle p_T^{\text{IC}} \rangle$	$\epsilon_p$	$\epsilon_p$	
–	–	$1.39 \times 10^{-1} \pm 3.5 \times 10^{-3}$	<b>0.00</b>	–	–	–	–	0.680
$5.60 \times 10^{-2} \pm 4.7 \times 10^{-3}$	<b>0.00</b>	$9.19 \times 10^{-2} \pm 5.1 \times 10^{-3}$	<b>0.00</b>	–	–	–	–	0.732
–	–	$3.53 \times 10^{-2} \pm 6.0 \times 10^{-3}$	<b>0.00</b>	$1.42 \times 10^{-6} \pm 7.2 \times 10^{-8}$	<b>0.00</b>	–	–	0.789
–	–	$8.84 \times 10^{-2} \pm 5.1 \times 10^{-3}$	<b>0.00</b>	–	–	$9.64 \times 10^{-1} \pm 7.6 \times 10^{-2}$	<b>0.00</b>	0.737
$3.62 \times 10^{-2} \pm 5.1 \times 10^{-3}$	<b>0.00</b>	$7.26 \times 10^{-2} \pm 5.4 \times 10^{-3}$	<b>0.00</b>	–	–	$6.84 \times 10^{-1} \pm 8.3 \times 10^{-2}$	<b>0.00</b>	0.754
$4.33 \times 10^{-3} \pm 5.5 \times 10^{-3}$	$4.30 \times 10^{-1}$	$3.52 \times 10^{-2} \pm 6.0 \times 10^{-3}$	<b>0.00</b>	$1.28 \times 10^{-6} \pm 1.1 \times 10^{-7}$	<b>0.00</b>	$1.29 \times 10^{-1} \pm 9.1 \times 10^{-2}$	$1.58 \times 10^{-1}$	0.790

TABLE VII. Regression results for  $v_2$  with IP-Glasma at 20–30% centrality,  $\sqrt{s_{NN}} = 200$  GeV.

Coefficient	$p$ value	Coefficient	$p$ value	Coefficient	$p$ value	Coefficient	$p$ value	$r^2$
$\epsilon_2$	$\epsilon_2$	$\epsilon_3$	$\epsilon_3$	$\langle p_T^{\text{IC}} \rangle$	$\langle p_T^{\text{IC}} \rangle$	$\epsilon_p$	$\epsilon_p$	
$2.77 \times 10^{-1} \pm 3.8 \times 10^{-3}$	<b>0.00</b>	–	–	–	–	–	–	0.879
$2.21 \times 10^{-1} \pm 6.6 \times 10^{-3}$	<b>0.00</b>	$1.08 \times 10^{-1} \pm 1.1 \times 10^{-2}$	<b>0.00</b>	–	–	–	–	0.894
$1.26 \times 10^{-1} \pm 7.8 \times 10^{-3}$	<b>0.00</b>	–	–	$1.17 \times 10^{-5} \pm 5.6 \times 10^{-7}$	<b>0.00</b>	–	–	0.924
$2.26 \times 10^{-1} \pm 6.5 \times 10^{-3}$	<b>0.00</b>	–	–	–	–	$1.84 \pm 2.0 \times 10^{-1}$	<b>0.00</b>	0.892
$1.92 \times 10^{-1} \pm 7.5 \times 10^{-3}$	<b>0.00</b>	$8.79 \times 10^{-2} \pm 1.1 \times 10^{-2}$	<b>0.00</b>	–	–	$1.43 \pm 1.9 \times 10^{-1}$	<b>0.00</b>	0.901
$1.19 \times 10^{-1} \pm 8.1 \times 10^{-3}$	<b>0.00</b>	$2.47 \times 10^{-2} \pm 1.0 \times 10^{-2}$	$1.57 \times 10^{-2}$	$1.04 \times 10^{-5} \pm 6.8 \times 10^{-7}$	<b>0.00</b>	$3.97 \times 10^{-1} \pm 1.8 \times 10^{-1}$	$2.98 \times 10^{-2}$	0.925

TABLE VIII. Regression results for  $v_3$  with IP-Glasma at 20–30% centrality,  $\sqrt{s_{NN}} = 200$  GeV.

Coefficient	$p$ value	Coefficient	$p$ value	Coefficient	$p$ value	Coefficient	$p$ value	
$\epsilon_2$	$\epsilon_2$	$\epsilon_3$	$\epsilon_3$	$\langle p_T^{\text{IC}} \rangle$	$\langle p_T^{\text{IC}} \rangle$	$\epsilon_p$	$\epsilon_p$	$r^2$
–	–	$1.45 \times 10^{-1} \pm 3.3 \times 10^{-3}$	<b>0.00</b>	–	–	–	–	0.725
$5.47 \times 10^{-2} \pm 3.2 \times 10^{-3}$	<b>0.00</b>	$7.04 \times 10^{-2} \pm 5.2 \times 10^{-3}$	<b>0.00</b>	–	–	–	–	0.801
–	–	$5.06 \times 10^{-2} \pm 5.5 \times 10^{-3}$	<b>0.00</b>	$4.78 \times 10^{-6} \pm 2.4 \times 10^{-7}$	<b>0.00</b>	–	–	0.818
–	–	$9.84 \times 10^{-2} \pm 4.8 \times 10^{-3}$	<b>0.00</b>	–	–	$1.12 \pm 8.9 \times 10^{-2}$	<b>0.00</b>	0.773
$4.41 \times 10^{-2} \pm 3.7 \times 10^{-3}$	<b>0.00</b>	$6.31 \times 10^{-2} \pm 5.3 \times 10^{-3}$	<b>0.00</b>	–	–	$5.19 \times 10^{-1} \pm 9.7 \times 10^{-2}$	<b>0.00</b>	0.808
$2.19 \times 10^{-2} \pm 4.4 \times 10^{-3}$	<b>0.00</b>	$4.38 \times 10^{-2} \pm 5.5 \times 10^{-3}$	<b>0.00</b>	$3.18 \times 10^{-6} \pm 3.7 \times 10^{-7}$	<b>0.00</b>	$2.03 \times 10^{-1} \pm 9.9 \times 10^{-2}$	$4.02 \times 10^{-2}$	0.826

#### 4. Configuration details

For each setup presented, unless stated otherwise, 750 event-by-event viscous hydrodynamics events were generated per centrality class, each initialized from a separate initial-state event. The IP-Glasma events were generated by running the glasma evolution until  $\tau = 0.5$  fm, which is identical to the passing time of SMASH IC at 200 GeV. From the resulting freeze-out hypersurface 1000 events are sampled for the hadronic afterburner evolution, in order to average out final-state effects. Unless stated otherwise, the code versions SMASH-vHLL-*hybrid*:298ebfa, vHLL-*0a10d56*, SMASH-2.2, vHLL-*params*:4bfe48a and SMASH-hadron-sampler-1.1 are used in this work. As pointed out above, the whole evolution for all three initial conditions is identical once the hydrodynamic stage has been reached, as the same viscosity, equation of state, switching energy density, etc., are chosen. The initial profiles are normalized such that the integrated energy of the fluid is the same as the energy deposited by the participants of the collision.

### III. RESULTS

In the following, we compare results based on the following properties of the different initial-state models:

- (i) The initial elliptic and triangular eccentricities of the energy densities generated by the initial condition model,  $\epsilon_2$  and  $\epsilon_3$ , which are calculated by integrating on the grid

$$\epsilon_n = \frac{\int r^n \epsilon(\mathbf{r}) e^{in\phi} d\mathbf{r}}{\int r^n \epsilon(\mathbf{r}) d\mathbf{r}} \quad (8)$$

with the energy density in the grid cell at  $\mathbf{r}$ ,  $\epsilon(\mathbf{r})$ . We restrict this to a 2D integration at midrapidity.

- (ii) The final-state elliptic and triangular flow of charged hadrons, calculated from the scalar product method [67],  $v_2$  and  $v_3$ .
- (iii) The final-state transverse flow at midrapidity,  $\langle p_T \rangle$ .
- (iv) In the case of the SMASH and IP-Glasma initial condition, the average initial-state radial flow,  $\langle p_T^{\text{IC}} \rangle$ , calculated directly from the momentum of initial-state

particles for SMASH and from the energy-momentum tensor for IP-Glasma as  $\sqrt{T_{xx}^2 + T_{yy}^2}$

- (v) In the case of the SMASH initial condition, the initial-state elliptic and triangular flow, calculated from the particles in the initial-state using the scalar product method [67],  $v_2^{\text{IC}}$  and  $v_3^{\text{IC}}$ .
- (vi) In the case of the IP-Glasma initial condition, the initial-state momentum anisotropy,  $\epsilon_p$  as defined in Ref. [68].

Flows and eccentricities were calculated using the software package SPARKX in the version 1.1 [69].

It is important to note that the results in the following comparison are dependent on the parameters chosen for each of the models. T<sub>R</sub>ENTo is a parametric model, and SMASH IC has smoothing parameters. By changing parameters, differences between the models can increase or decrease. However, we fixed the parameters of these models by the agreement with experimental data. We therefore compare the initial condition models under the assumption that parameters are chosen which lead to minimal tension with experimental data.

#### A. Averaged quantities

Figures 1–3 show  $\epsilon_2$  and  $\epsilon_3$  as a function of the impact parameter for three experimentally relevant systems: Au-Au collisions at  $\sqrt{s_{NN}} = 200$  GeV, Pb-Pb collisions at  $\sqrt{s_{NN}} = 5020$  GeV and O-O collisions at  $\sqrt{s_{NN}} = 7$  TeV. As T<sub>R</sub>ENTo does not provide oxygen configurations, they were taken from Ref. [70]. For all these systems, the passing time is 0.5 fm/ $c$ . For both Au-Au collisions at  $\sqrt{s_{NN}} = 200$  GeV and Pb-Pb collisions at  $\sqrt{s_{NN}} = 5020$  GeV, the three models give similar results with comparable increase as a function of the impact parameter. In both cases, IP-Glasma produces the highest values for the eccentricities, expect for  $\epsilon_3$  in very peripheral collisions at high energies, where SMASH gives slightly higher values. Similarly as has been observed in Ref. [71], even for almost central collisions the eccentricity stays finite, especially for IP-Glasma. A good agreement between predictions for eccentricities between different models has been also observed in Ref. [72]. This changes substantially when

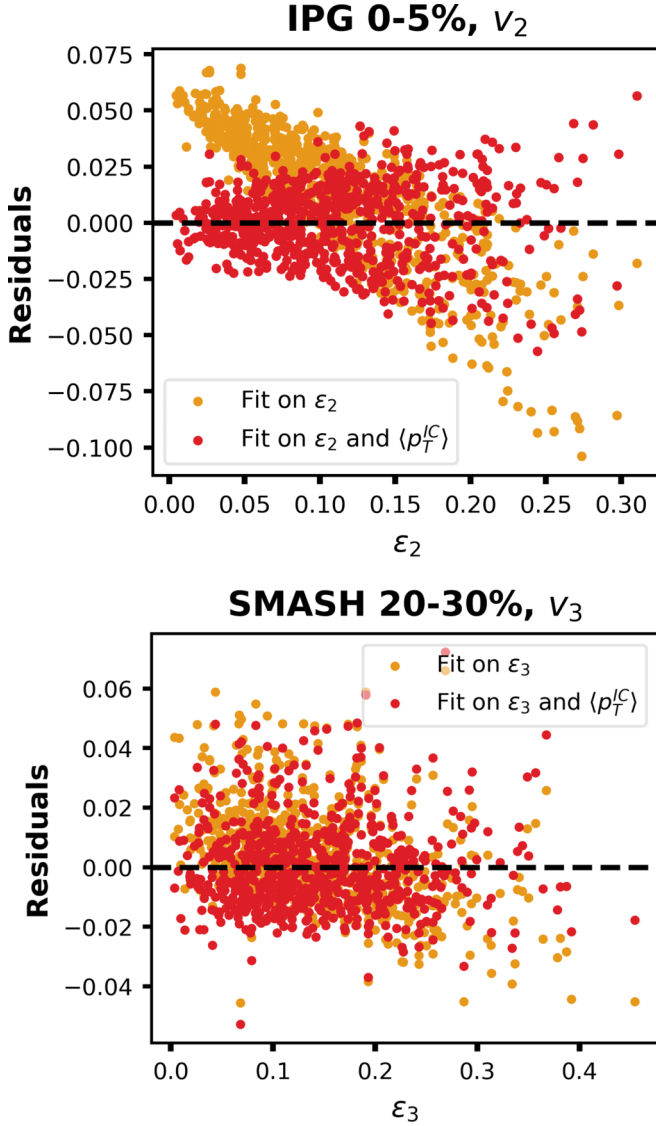


FIG. 10. Residuals between observed and fitted values for a fit on  $\epsilon_2$ , on the one hand, and  $\epsilon_2$  and  $\langle p_T^C \rangle$ , on the other hand, for a simulation with IP-Glasma at 0–5% centrality (top). The same plot for midcentral collisions in SMASH, for the fit with  $v_3$  on  $\epsilon_3$  (bottom) for Au-Au collisions at  $\sqrt{s_{NN}} = 200$  GeV.

looking at small nuclei in Fig. 3. SMASH and IP-Glasma are still comparable, but T<sub>R</sub>ENTo gives now much more spherical profiles with only small impact-parameter dependence. In the following, we restrict ourselves to  $\sqrt{s_{NN}} = 200$  GeV in order to limit computational costs while at the same time achieving statistically significant statements. Figures 4 and 5 show the averaged values of  $\epsilon_2$ ,  $\epsilon_3$ ,  $v_2$ , and  $v_3$  for the three models for Au-Au collisions at  $\sqrt{s_{NN}} = 200$  GeV at 0–5% and 20–30% centrality, respectively. As expected from Fig. 1, the eccentricities of the models have similar values in both centrality classes. Especially T<sub>R</sub>ENTo and the transport IC lead to similar values of final-state flow, as was also seen at lower energies in Ref. [48]. However, the SMASH IC here leads to slightly greater flow than T<sub>R</sub>ENTo. The differences are slightly greater for the final-state flow, which is in general

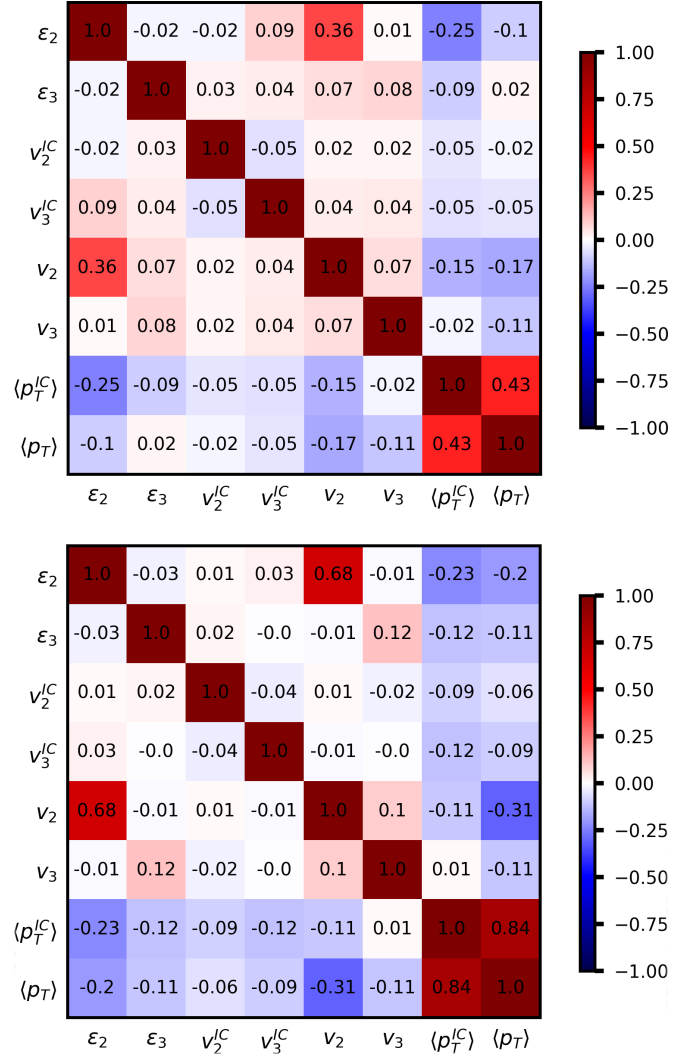


FIG. 11. Pearson correlation matrix for SMASH at  $\sqrt{s_{NN}} = 17.3$  GeV at 0–5% centrality (top) and 20–30% centrality (bottom).

greater when IP-Glasma is employed as an initial-state model, especially for central collisions. Although this suggests that the models produce comparable results, more intricate differences arise when looking at the response function in Fig. 6. Although the only change in the three setups is the choice of the initial condition model, the response to initial-state eccentricities differs, especially at low eccentricities. Deeper insights into this can be gained by looking into the distribution of the variables in an event-by-event basis. It was also observed earlier that while the average eccentricities between different models might agree, this is not necessarily given for the distribution of eccentricities [72].

## B. Event-by-event distributions

Figures 7 and 8 show the eccentricity and flow distribution, respectively. In the case of eccentricities, we see that SMASH has a lot more peaked distribution of eccentricities, especially at central collisions, where the distribution for IP-Glasma and T<sub>R</sub>ENTo is very similar. This changes for

TABLE IX. Regression results for  $v_2$  with SMASH IC at 0–5% centrality,  $\sqrt{s_{NN}} = 17.3$  GeV.

Coefficient	$p$ value	Coefficient	$p$ value	Coefficient	$p$ value	Coefficient	$p$ value	Coefficient	$p$ value	$r^2$
$\epsilon_2$	$\epsilon_2$	$\epsilon_3$	$\epsilon_3$	$\langle p_T^{\text{IC}} \rangle$	$\langle p_T^{\text{IC}} \rangle$	$v_2^{\text{IC}}$	$v_2^{\text{IC}}$	$v_3^{\text{IC}}$	$v_3^{\text{IC}}$	
$2.52 \times 10^{-1} \pm 7.3 \times 10^{-3}$	<b>0.00</b>	–	–	–	–	–	–	–	–	0.616
$1.96 \times 10^{-1} \pm 1.1 \times 10^{-2}$	<b>0.00</b>	$7.88 \times 10^{-2} \pm 1.2 \times 10^{-2}$	<b>0.00</b>	–	–	–	–	–	–	0.636
$1.67 \times 10^{-1} \pm 1.4 \times 10^{-2}$	<b>0.00</b>	–	–	$9.01 \times 10^{-6} \pm 1.3 \times 10^{-6}$	<b>0.00</b>	–	–	–	–	0.638
$2.04 \times 10^{-1} \pm 1.1 \times 10^{-2}$	<b>0.00</b>	–	–	–	–	$1.85 \times 10^{-1} \pm 3.4 \times 10^{-2}$	<b>0.00</b>	–	–	0.630
$1.75 \times 10^{-1} \pm 1.3 \times 10^{-2}$	<b>0.00</b>	$5.44 \times 10^{-2} \pm 1.5 \times 10^{-2}$	<b>0.00</b>	–	–	$9.14 \times 10^{-2} \pm 4.0 \times 10^{-2}$	$2.18 \times 10^{-2}$	$6.02 \times 10^{-2} \pm 4.7 \times 10^{-2}$	$1.98 \times 10^{-1}$	0.640
$1.65 \times 10^{-1} \pm 1.5 \times 10^{-2}$	<b>0.00</b>	$4.13 \times 10^{-2} \pm 1.6 \times 10^{-2}$	$2.22 \times 10^{-2}$	$4.32 \times 10^{-6} \pm 2.4 \times 10^{-6}$	$7.07 \times 10^{-2}$	$4.98 \times 10^{-2} \pm 4.6 \times 10^{-2}$	$2.79 \times 10^{-1}$	$1.70 \times 10^{-2} \pm 5.2 \times 10^{-2}$	$7.46 \times 10^{-1}$	0.642

off-central collisions, where the distribution of SMASH stays more peaked for  $\epsilon_2$ , but becomes comparable to T<sub>R</sub>ENTo for  $\epsilon_3$ . In both cases, IP-Glasma is spread out considerably wider. For both centralities and all three models, there is no significant  $\epsilon_2$ - $\epsilon_3$  correlation, and the spread in  $\epsilon_2$  is greater than for  $\epsilon_3$ . Although final-state flows are often seen as a linear response to initial-state eccentricities, the initial-state distributions vary in their behavior from the final-state properties. For both centrality classes, the distributions for the T<sub>R</sub>ENTo model are more peaked than the results with SMASH and IP-Glasma. Additionally, we now observe significant correlations, as can be seen in the orientations of the ellipses at the lower left corner. SMASH and IP-Glasma results show a positive correlation between  $v_2$  and  $v_3$ , whereas T<sub>R</sub>ENTo exhibits a negative correlation for central events. This shows that the properties of final-state flow cannot be exclusively reduced to the initial-state eccentricities, even if other elements of the hybrid approach are fixed. In the following, we take a look at possible candidates to explain the deviations between the models.

### C. Pearson correlations

Figure 9 shows the Pearson correlation matrix for all relevant quantities for all three models at the studied centrality classes. We find here also the observed correlations from Figs. 7 and 8. Regarding the  $\epsilon_n$ - $v_n$ -correlations, we observe that these are in general the strongest for T<sub>R</sub>ENTo and SMASH. For IP-Glasma, they become especially weak for central collisions, which can be explained by the higher granularity of the IP-Glasma initial conditions and therefore the higher impact of fluctuations. Whereas they increase both for T<sub>R</sub>ENTo and IP-Glasma when going to more off-central collisions, they decrease in the case of SMASH. In comparison with Ref. [73], where it was found that in general, the correlation  $\epsilon_n$ - $v_n$  increases for more off-central collisions using NeXus events, we see that this can not be generalized to all initial condition models. For SMASH, we see that the initial-state flows do not exhibit any significant correlation with final-state or initial-state observables. The case is less clear for central IP-Glasma events, where the correlation

 TABLE X. Regression results for  $v_3$  with SMASH IC at 0–5% centrality,  $\sqrt{s_{NN}} = 17.3$  GeV.

Coefficient	$p$ value	Coefficient	$p$ value	Coefficient	$p$ value	Coefficient	$p$ value	Coefficient	$p$ value	$r^2$
$\epsilon_2$	$\epsilon_2$	$\epsilon_3$	$\epsilon_3$	$\langle p_T^{\text{IC}} \rangle$	$\langle p_T^{\text{IC}} \rangle$	$v_2^{\text{IC}}$	$v_2^{\text{IC}}$	$v_3^{\text{IC}}$	$v_3^{\text{IC}}$	
–	–	$1.01 \times 10^{-1} \pm 1.1 \times 10^{-2}$	<b>0.00</b>	–	–	–	–	–	–	0.097
$2.78 \times 10^{-2} \pm 1.6 \times 10^{-2}$	$8.83 \times 10^{-2}$	$7.71 \times 10^{-2} \pm 1.8 \times 10^{-2}$	<b>0.00</b>	–	–	–	–	–	–	0.101
–	–	$5.42 \times 10^{-2} \pm 2.4 \times 10^{-2}$	$2.29 \times 10^{-2}$	$4.44 \times 10^{-6} \pm 2.0 \times 10^{-6}$	$2.73 \times 10^{-2}$	–	–	–	–	0.103
–	–	$7.33 \times 10^{-2} \pm 1.8 \times 10^{-2}$	<b>0.00</b>	–	–	$9.44 \times 10^{-2} \pm 5.1 \times 10^{-2}$	$6.25 \times 10^{-2}$	–	–	0.102
$8.21 \times 10^{-3} \pm 1.9 \times 10^{-2}$	$6.73 \times 10^{-1}$	$5.53 \times 10^{-2} \pm 2.1 \times 10^{-2}$	<b>0.01</b>	–	–	$5.11 \times 10^{-2} \pm 5.8 \times 10^{-2}$	$3.76 \times 10^{-1}$	$9.06 \times 10^{-2} \pm 6.8 \times 10^{-2}$	$1.81 \times 10^{-1}$	0.105
$5.26 \times 10^{-3} \pm 2.1 \times 10^{-2}$	$8.04 \times 10^{-1}$	$5.16 \times 10^{-2} \pm 2.4 \times 10^{-2}$	$3.09 \times 10^{-2}$	$1.22 \times 10^{-6} \pm 3.5 \times 10^{-6}$	$7.25 \times 10^{-1}$	$3.93 \times 10^{-2} \pm 6.7 \times 10^{-2}$	$5.56 \times 10^{-1}$	$7.85 \times 10^{-2} \pm 7.6 \times 10^{-2}$	$3.03 \times 10^{-1}$	0.105

TABLE XI. Regression results for  $v_2$  with SMASH IC at 20–30% centrality,  $\sqrt{s_{NN}} = 17.3$  GeV.

Coefficient	$p$ value	Coefficient	$p$ value	Coefficient	$p$ value	Coefficient	$p$ value	Coefficient	$p$ value	$r^2$
$\epsilon_2$	$\epsilon_2$	$\epsilon_3$	$\epsilon_3$	$\langle p_T^{\text{IC}} \rangle$	$\langle p_T^{\text{IC}} \rangle$	$v_2^{\text{IC}}$	$v_2^{\text{IC}}$	$v_3^{\text{IC}}$	$v_3^{\text{IC}}$	
$2.11 \times 10^{-1} \pm 2.2 \times 10^{-3}$	<b>0.00</b>	–	–	–	–	–	–	–	–	0.922
$1.94 \times 10^{-1} \pm 3.9 \times 10^{-3}$	<b>0.00</b>	$3.92 \times 10^{-2} \pm 7.6 \times 10^{-3}$	<b>0.00</b>	–	–	–	–	–	–	0.925
$1.63 \times 10^{-1} \pm 5.6 \times 10^{-3}$	<b>0.00</b>	–	–	$3.09 \times 10^{-5} \pm 3.3 \times 10^{-6}$	<b>0.00</b>	–	–	–	–	0.930
$1.94 \times 10^{-1} \pm 4.0 \times 10^{-3}$	<b>0.00</b>	–	–	–	–	$1.23 \times 10^{-1} \pm 2.5 \times 10^{-2}$	<b>0.00</b>	–	–	0.925
$1.82 \times 10^{-1} \pm 5.0 \times 10^{-3}$	<b>0.00</b>	$2.73 \times 10^{-2} \pm 8.1 \times 10^{-3}$	<b>0.00</b>	–	–	$8.37 \times 10^{-2} \pm 2.6 \times 10^{-2}$	<b>0.00</b>	$4.83 \times 10^{-2} \pm 2.8 \times 10^{-2}$	$8.62 \times 10^{-2}$	0.927
$1.62 \times 10^{-1} \pm 5.7 \times 10^{-3}$	<b>0.00</b>	$7.30 \times 10^{-3} \pm 8.5 \times 10^{-3}$	$3.88 \times 10^{-1}$	$2.96 \times 10^{-5} \pm 4.5 \times 10^{-6}$	<b>0.00</b>	$1.37 \times 10^{-2} \pm 2.8 \times 10^{-2}$	$6.20 \times 10^{-1}$	$-2.11 \times 10^{-2} \pm 2.9 \times 10^{-2}$	$4.73 \times 10^{-1}$	0.931

between  $\epsilon_p$  and  $v_2$  becomes of the same magnitude as the  $\epsilon_2$ - $v_2$  correlation, albeit both at a very low level. This is in line with the observation in Ref. [68], which observed a opposite behavior of  $\epsilon_p$  and  $v_2$  as a function of multiplicity. It was also observed in Ref. [74] that classifying the initial state by eccentricities, average square radius of the initial state as well as total energy per unit rapidity can be used to predict final-state flows well, which is in line with our observation that there is no correlation between initial-state and final-state momentum anisotropy. Looking at the final-state transverse momentum, the picture is very different for the three models. In the case of TRENTo, it is slightly anticorrelated with all initial- and final-state properties in the central collision, and even stronger anticorrelated at off-central collisions. In SMASH on the other hand, a strong anticorrelation is only observed towards final flows, and in the case of IP-Glasma, no significant correlation is observed. It is noteworthy that SMASH exhibits a significant correlation between radial flow and final transverse momentum, much stronger than what one finds for IP-Glasma. SMASH additionally shows a slight anticorrelation between initial-state eccentricities and the radial flow. The initial ellipticity is negatively correlated to the inverse root-mean-square

radius. Smaller, more compact sources give larger transverse momentum but a smaller deformation.

#### D. Regression

The assumption of a linear relationship between initial eccentricities and final-state flow can be seen as applying a linear regression model. Due to our access to additional initial-state properties, we can test whether further initial-state properties contribute to the emergence of final-state flow, apart from the relevant eccentricity mode. It is important to stress that it is not sufficient to only study the correlations for this, as correlations only capture the relationship between two variables, but we are interested in a multiple linear statement. This can be clarified in a simple example. Assume that there are two initial-state properties both contributing to  $v_q$  with  $v_q = 2\epsilon_p + \epsilon_q$ , and both initial-state properties being perfectly anticorrelated. Although  $\epsilon_q$  is also a source of  $v_q$ , depending on the data at hand, the Pearson correlation will be negative, as the effect is shadowed by the stronger contribution of  $\epsilon_p$ . For the SMASH and IP-Glasma initial conditions at both studied centrality classes, a selection of linear regressions on different

TABLE XII. Regression results for  $v_3$  with SMASH IC at 20–30% centrality,  $\sqrt{s_{NN}} = 17.3$  GeV.

Coefficient	$p$ value	Coefficient	$p$ value	Coefficient	$p$ value	Coefficient	$p$ value	Coefficient	$p$ value	$r^2$
$\epsilon_2$	$\epsilon_2$	$\epsilon_3$	$\epsilon_3$	$\langle p_T^{\text{IC}} \rangle$	$\langle p_T^{\text{IC}} \rangle$	$v_2^{\text{IC}}$	$v_2^{\text{IC}}$	$v_3^{\text{IC}}$	$v_3^{\text{IC}}$	
–	–	$6.38 \times 10^{-2} \pm 4.9 \times 10^{-3}$	<b>0.00</b>	–	–	–	–	–	–	0.184
$1.09 \times 10^{-2} \pm 4.4 \times 10^{-3}$	$1.34 \times 10^{-2}$	$4.62 \times 10^{-2} \pm 8.6 \times 10^{-3}$	<b>0.00</b>	–	–	–	–	–	–	0.190
–	–	$3.57 \times 10^{-2} \pm 9.8 \times 10^{-3}$	<b>0.00</b>	$9.79 \times 10^{-6} \pm 3.0 \times 10^{-6}$	<b>0.00</b>	–	–	–	–	0.195
–	–	$5.36 \times 10^{-2} \pm 8.0 \times 10^{-3}$	<b>0.00</b>	–	–	$4.03 \times 10^{-2} \pm 2.5 \times 10^{-2}$	$1.06 \times 10^{-1}$	–	–	0.187
$7.93 \times 10^{-3} \pm 5.8 \times 10^{-3}$	$1.70 \times 10^{-1}$	$4.34 \times 10^{-2} \pm 9.3 \times 10^{-3}$	<b>0.00</b>	–	–	$4.53 \times 10^{-3} \pm 3.0 \times 10^{-2}$	$8.81 \times 10^{-1}$	$2.80 \times 10^{-2} \pm 3.2 \times 10^{-2}$	$3.86 \times 10^{-1}$	0.191
$8.43 \times 10^{-4} \pm 6.7 \times 10^{-3}$	$9.01 \times 10^{-1}$	$3.62 \times 10^{-2} \pm 1.0 \times 10^{-2}$	<b>0.00</b>	$1.08 \times 10^{-5} \pm 5.3 \times 10^{-6}$	$4.19 \times 10^{-2}$	$-2.09 \times 10^{-2} \pm 3.3 \times 10^{-2}$	$5.22 \times 10^{-1}$	$2.79 \times 10^{-3} \pm 3.5 \times 10^{-2}$	$9.36 \times 10^{-1}$	0.196

initial-state properties for both  $v_2$  and  $v_3$  are given in the Appendix. For all used explanatory data, we report the result of the coefficient as well as the  $p$  value, which gives the probability of receiving the outcome under the null hypothesis. As a rule of thumb, a  $p$  value smaller than 0.05 is necessary but not sufficient to consider the inclusion a dependent variable as statistically significant. Additionally we report  $r^2$ , which is a common measure on how well the resulting model manages to predict the dependent variable.  $r^2$  is the proportion of the variation of the dependent variable that is predictable from the independent variables on the basis of the model. Adding further independent variables is always expected to slightly improve  $r^2$ . For all the observed cases, we can, however, determine that the inclusion of  $\langle p_T^{\text{IC}} \rangle$  is statistically significant and improves  $r^2$  considerably more than the inclusion of any of the other independent variables. We can see in Tables I–IV that the effect is especially strong for IP-Glasma, which contains a significant amount of transverse momentum. However, Tables V–VIII show that the effect, albeit smaller, is qualitatively similar for SMASH. Due to this consistent and significant improvement, it becomes clear that the radial flow in the initial state is a next-to-leading order contribution to final-state flows. A stronger transverse push yields a stronger hydrodynamic response of the spectra to the initial azimuthal deformation. The strength of the improvement in  $r^2$  is generally stronger for IP-Glasma due to its higher radial flow. This explains the differences in the response functions observed earlier: Depending on the initial condition model, the presence of initial-state transverse flow modifies the response to initial-state eccentricities. The eccentricity alone is not the only aspect of the initial state which determines initial-state flow. The effect of including radial flow in the predictor of final-state flow becomes clear in Fig. 10. Here we show the residuals of the prediction of the linear regression model with respect to the observed value in two cases where the improvement by including a second independent variable was especially significant. In both cases, this compensates to high predictions of flow for small eccentricities, and too small predictions for the flow at high eccentricities. For events with small eccentricities, radial flow becomes the main contribution to the final flow.

### E. SMASH at intermediate energies

As the SMASH IC is a three-dimensional initial condition model, it can be also applied to lower collision energies. Therefore, we can extend the study of this initial condition model also to the case of PbPb @  $\sqrt{s_{NN}} = 17.3$  GeV, where the passing time is 1.44 fm/c. The correlation matrix in Fig. 11 shows a weaker dependence between  $\epsilon_3$  and  $v_3$  in comparison to the high-energy case. Additionally, the correlation between the flow modes is also reduced, hinting at a stronger role of nonflow for  $v_3$ . We observe a greatly increased relationship between radial flow and final transverse flow, whereas the relationship between eccentricities and radial flow remains roughly unchanged. Again, tables of different linear regression models can be found in Tables IX–XII. Due to the weak  $\epsilon_3$ - $v_3$  correlation, linear regression with  $v_3$  as dependent variable fails to appropriately describe the data.

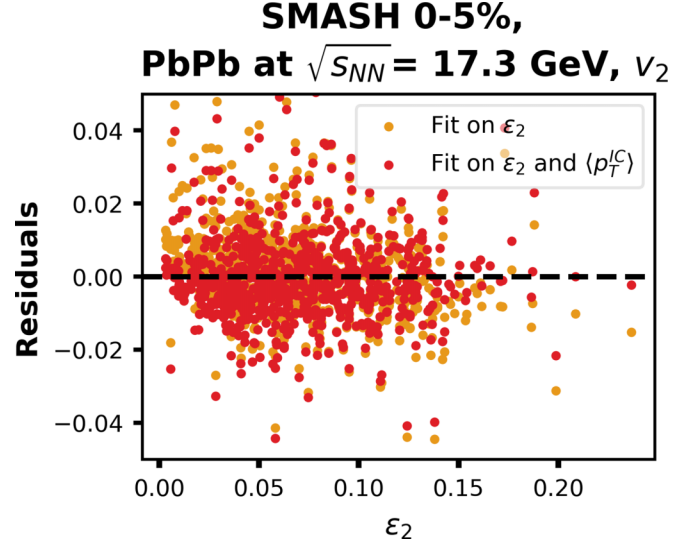


FIG. 12. Residuals between observed and fitted values for a fit on  $\epsilon_2$ , on the one hand, and  $\epsilon_2$  and  $\langle p_T^{\text{IC}} \rangle$ , on the other hand, for a simulation with SMASH at 0–5% centrality and  $\sqrt{s_{NN}} = 17.3$  GeV.

The including of radial flow in the linear fit again improves the regression, albeit at a smaller degree than for higher energies. The effect on the residuals remains the same than at higher energies, as can be seen in Fig. 12.

## IV. CONCLUSIONS AND OUTLOOK

In this work, we have presented a comparison between three different initial-state models, SMASH IC, T<sub>R</sub>ENTo, and IP-Glasma, in the context of a hybrid approach for simulating heavy-ion collisions. Although averaged quantities like eccentricities and final-state flows were found to be comparable across the models for large nuclei, significant differences emerged on studying distributions and correlations on an event-by-event basis.

The distributions of eccentricities and final-state flows were found to vary substantially between models, with T<sub>R</sub>ENTo exhibiting the most peaked distributions. This demonstrates that averaged values alone are insufficient to fully characterize differences between initial-state models. Additionally, the correlations between initial eccentricities and final flows were found to be noticeably model dependent, with the strongest correlations seen for T<sub>R</sub>ENTo and the weakest for IP-Glasma, especially in central collisions. Similarly, although the same hydrodynamic evolution was used in all cases, the response of the system to the initial eccentricities varied among the initial condition models.

This results from the observation that the transverse momentum in the initial state, as provided by SMASH IC and IP-Glasma, was found to non-negligibly affect final flows and therefore improves predictions of final flows when included alongside eccentricity in a linear regression model. This contribution from initial radial flow presents a relevant second-order effect when determining final anisotropic flows. This challenges the common assumption of a universal linear hydrodynamic response. Extending the analysis to lower en-

ergies using SMASH IC showed overall weaker correlations, however initial radial flow was still found to be beneficial for predicting final flows.

In contrast, the anisotropies of the initial-state momentum were shown to not affect final state in any significant way. This means that the initial state momentum anisotropies isotropize quickly during the hydrodynamic evolution and do not affect the momentum space of the final state.

In summary, this comprehensive event-by-event analysis has revealed significant differences between common initial-state models that are highly relevant when predicting final-state observables. While averaged values appear comparable between models, the event-by-event distributions, correlations, and hydrodynamic response differ substantially. Our results highlight the importance of initial transverse momentum as a contributor to final flows, emphasizing the need to characterize initial conditions beyond eccentricity alone when correlating to final-state observables.

Future studies could extend this analysis to further initial condition models. Most importantly, IP-Glasma can be combined with alternative approaches for the pre-equilibrium dynamics. Pre-equilibrium can have a substantial effect on the initial-state transverse momentum [75–78]. Alternatively, the study could be also performed in an anisotropic hydrodynamics setup [79], which could potentially improve model uncertainties at the point of fluidization. Additionally, it would be worthwhile to extend the study to further observables sensitive to the initial state. Next-to-higher-order flow coefficients, comparisons for 3D initial-state models [36,80,81] can also be performed on the decorrelation length of anisotropic flow [82]. Comparisons to other 3D initial-state models would also allow to perform studies at lower energies, which are the stronghold of SMASH IC.

Raw data of all figures can be downloaded from the Supplemental Material [83].

## ACKNOWLEDGMENTS

This work was supported by the Deutsche Forschungsgemeinschaft (DFG, German Research Foundation), Project No. 315477589–TRR 211. N.G. acknowledges support by the Stiftung Polytechnische Gesellschaft Frankfurt am Main as well as the Studienstiftung des Deutschen Volkes. Computational resources have been provided by the GreenCube at GSI.

## APPENDIX: REGRESSION TABLES

The following section contains the regression results for the different models and dependent variables, as well as different choices for the set of independent variables. Each row is an independent regression. For each independent variable, the coefficient with error was well as the  $p$  value is given. As a  $p$  value smaller than 0.05 is seen as statistically significant, it is printed in bold. If a value is present in the column of a row, then the respective independent variable was used in the regression. The final column contains the  $r^2$  value for the regression.

We observe throughout all models, independent variables, and centralities for  $\sqrt{s_{NN}} = 200$  GeV that the most significant increase in predictive power, measured by  $r^2$ , is gained by adding  $\langle p_T^{IC} \rangle$  as a second independent variable. Adding further variables is either not statistically significant, leading to greater  $p^2$  values, or only negligibly improves  $r^2$ , which is always expected to stay constant or improve on adding further independent variables. Using other independent variables apart from  $\epsilon_n$  and  $\langle p_T^{IC} \rangle$  fails to consistently reach improvements greater or equal to the combination of  $\epsilon_n$  and  $\langle p_T^{IC} \rangle$ .

- 
- [1] A. Adare *et al.* (PHENIX), *Phys. Rev. Lett.* **107**, 252301 (2011).
- [2] J. Adam *et al.* (STAR), *Phys. Rev. C* **72**, 014904 (2005).
- [3] H. Elfner and B. Müller, *J. Phys. G: Nucl. Part. Phys.* **50**, 103001 (2023).
- [4] J. Noronha-Hostler, L. Yan, F. G. Gardim, and J.-Y. Ollitrault, *Phys. Rev. C* **93**, 014909 (2016).
- [5] A. Schäfer, I. Karpenko, X.-Y. Wu, J. Hammelmann, and H. Elfner, *Eur. Phys. J. A* **58**, 230 (2022).
- [6] I. A. Karpenko, P. Huovinen, H. Petersen, and M. Bleicher, *Phys. Rev. C* **91**, 064901 (2015).
- [7] H. Petersen, J. Steinheimer, G. Burau, M. Bleicher, and H. Stöcker, *Phys. Rev. C* **78**, 044901 (2008).
- [8] X.-Y. Wu, G.-Y. Qin, L.-G. Pang, and X.-N. Wang, *Phys. Rev. C* **105**, 034909 (2022).
- [9] C. Shen, G. Denicol, C. Gale, S. Jeon, A. Monnai, and B. Schenke, *Nucl. Phys. A* **967**, 796 (2017).
- [10] Y. Akamatsu, M. Asakawa, T. Hirano, M. Kitazawa, K. Morita, K. Murase, Y. Nara, C. Nonaka, and A. Ohnishi, *Phys. Rev. C* **98**, 024909 (2018).
- [11] A. Nandi, L. Kumar, and N. Sharma, *Phys. Rev. C* **102**, 024902 (2020).
- [12] H. Petersen, *J. Phys. G: Nucl. Part. Phys.* **41**, 124005 (2014).
- [13] D. Everett *et al.* (JETSCAPE Collaboration), *Phys. Rev. C* **103**, 054904 (2021).
- [14] J. Ghiglieri, G. D. Moore, and D. Teaney, *J. High Energy Phys.* **03** (2018) 179.
- [15] J. Auvinen, K. J. Eskola, P. Huovinen, H. Niemi, R. Paatelainen, and P. Petreczky, *Phys. Rev. C* **102**, 044911 (2020).
- [16] G. Nijs, W. van der Schee, U. Gürsoy, and R. Snellings, *Phys. Rev. Lett.* **126**, 202301 (2021).
- [17] G. Nijs, W. van der Schee, U. Gürsoy, and R. Snellings, *Phys. Rev. C* **103**, 054909 (2021).
- [18] C. Greiner, J. Noronha-Hostler, and J. Noronha, *PoS* **135**, 033 (2011).
- [19] M. I. Gorenstein, M. Hauer, and O. N. Moroz, *Phys. Rev. C* **77**, 024911 (2008).
- [20] L. P. Csernai, J. I. Kapusta, and L. D. McLerran, *Phys. Rev. Lett.* **97**, 152303 (2006).
- [21] D. Liyanage, O. Sürer, M. Plumlee, S. M. Wild, and U. Heinz, *Phys. Rev. C* **108**, 054905 (2023).
- [22] D. Everett *et al.* (JETSCAPE Collaboration), *Phys. Rev. Lett.* **126**, 242301 (2021).

- [23] P. F. Kolb, U. W. Heinz, P. Huovinen, K. J. Eskola, and K. Tuominen, *Nucl. Phys. A* **696**, 197 (2001).
- [24] J. Bartels, K. J. Golec-Biernat, and H. Kowalski, *Phys. Rev. D* **66**, 014001 (2002).
- [25] H. Kowalski and D. Teaney, *Phys. Rev. D* **68**, 114005 (2003).
- [26] Z.-W. Lin, C. M. Ko, B.-A. Li, B. Zhang, and S. Pal, *Phys. Rev. C* **72**, 064901 (2005).
- [27] T. Hirano, U. W. Heinz, D. Kharzeev, R. Lacey, and Y. Nara, *Phys. Lett. B* **636**, 299 (2006).
- [28] A. Adil, H.-J. Drescher, A. Dumitru, A. Hayashigaki, and Y. Nara, *Phys. Rev. C* **74**, 044905 (2006).
- [29] H.-J. Drescher and Y. Nara, *Phys. Rev. C* **75**, 034905 (2007).
- [30] K. Werner, I. Karpenko, T. Pierog, M. Bleicher, and K. Mikhailov, *Phys. Rev. C* **82**, 044904 (2010).
- [31] A. Accardi, J. L. Albacete, M. Anselmino, N. Armesto, E. C. Aschenauer, A. Bacchetta, D. Boer, W. K. Brooks, T. Burton, N.-B. Chang, W.-T. Deng, A. Deshpande, M. Diehl, A. Dumitru, R. Dupré, R. Ent, S. Fazio, H. Gao, V. Guzey, H. Hakobyan *et al.*, *Eur. Phys. J. A* **52**, 268 (2016).
- [32] B. Schenke, P. Tribedy, and R. Venugopalan, *Phys. Rev. Lett.* **108**, 252301 (2012).
- [33] M. Rybczynski, G. Stefanek, W. Broniowski, and P. Bozek, *Comput. Phys. Commun.* **185**, 1759 (2014).
- [34] J. S. Moreland, J. E. Bernhard, and S. A. Bass, *Phys. Rev. C* **92**, 011901(R) (2015).
- [35] W. van der Schee and B. Schenke, *Phys. Rev. C* **92**, 064907 (2015).
- [36] O. Garcia-Montero, H. Elfner, and S. Schlichting, *Phys. Rev. C* **109**, 044916 (2024).
- [37] H. Holopainen, H. Niemi, and K. J. Eskola, *Phys. Rev. C* **83**, 034901 (2011).
- [38] H. Song, S. A. Bass, U. Heinz, T. Hirano, and C. Shen, *Phys. Rev. Lett.* **106**, 192301(E) (2011); **109**, 139904(E) (2012).
- [39] <https://github.com/smash-transport/smash-vhllh-hybrid>.
- [40] I. Karpenko, P. Huovinen, and M. Bleicher, *Comput. Phys. Commun.* **185**, 3016 (2014).
- [41] G. S. Denicol, S. Jeon, and C. Gale, *Phys. Rev. C* **90**, 024912 (2014).
- [42] S. Ryu, J.-F. Paquet, C. Shen, G. S. Denicol, B. Schenke, S. Jeon, and C. Gale, *Phys. Rev. Lett.* **115**, 132301 (2015).
- [43] J. Steinheimer, S. Schramm, and H. Stoecker, *Phys. Rev. C* **84**, 045208 (2011).
- [44] A. Motornenko, J. Steinheimer, V. Vovchenko, S. Schramm, and H. Stoecker, *Phys. Rev. C* **101**, 034904 (2020).
- [45] E. R. Most, A. Motornenko, J. Steinheimer, V. Dexheimer, M. Hanauske, L. Rezzolla, and H. Stoecker, *Phys. Rev. D* **107**, 043034 (2023).
- [46] P. Huovinen and H. Petersen, *Eur. Phys. J. A* **48**, 171 (2012).
- [47] N. Götz and H. Elfner, *Phys. Rev. C* **106**, 054904 (2022).
- [48] J. Cimerman, I. Karpenko, B. Tomášik, and B. A. Trzeciak, *Phys. Rev. C* **103**, 034902 (2021).
- [49] <https://github.com/smash-transport/smash-hadron-sampler>.
- [50] F. Cooper, G. Frye, and E. Schonberg, *Phys. Rev. D* **11**, 192 (1975).
- [51] J. Weil, V. Steinberg, J. Staudenmaier, L. G. Pang, D. Oliinychenko, J. Mohs, M. Kretz, T. Kehrenberg, A. Goldschmidt, B. Bäuchle, J. Auvinen, M. Attems, and H. Petersen, *Phys. Rev. C* **94**, 054905 (2016).
- [52] D. Oliinychenko, V. Steinberg, J. Staudenmaier, J. Weil, A. Schäfer, H. E. (Petersen), S. Ryu, J. Mohs, F. Li, A. Sorensen, D. Mitrovic, L. Pang, A. Sciarra, O. Garcia-Montero, M. Mayer, N. Kübler, and Nikita, *smash-transport/smash: SMASH-2.1*, Zenodo 2021, <https://doi.org/10.5281/zenodo.5796168>.
- [53] <https://smash-transport.github.io/>.
- [54] M. Tanabashi *et al.* (Particle Data Group), *Phys. Rev. D* **98**, 030001 (2018).
- [55] T. Sjöstrand, S. Mrenna, and P. Skands, *Comput. Phys. Commun.* **178**, 852 (2008).
- [56] D. Oliinychenko and H. Petersen, *Phys. Rev. C* **93**, 034905 (2016).
- [57] G. Inghirami and H. Elfner, *Eur. Phys. J. C* **82**, 796 (2022).
- [58] J. Auvinen and H. Petersen, *Phys. Rev. C* **88**, 064908 (2013).
- [59] D. Everett *et al.* (JETSCAPE), *Phys. Rev. C* **106**, 064901 (2022).
- [60] J. E. Bernhard, J. S. Moreland, and S. A. Bass, *Nat. Phys.* **15**, 1113 (2019).
- [61] J. E. Bernhard, J. S. Moreland, S. A. Bass, J. Liu, and U. Heinz, *Phys. Rev. C* **94**, 024907 (2016).
- [62] F. Gelis, E. Iancu, J. Jalilian-Marian, and R. Venugopalan, *Annu. Rev. Nucl. Part. Sci.* **60**, 463 (2010).
- [63] A. Krasnitz and R. Venugopalan, *Nucl. Phys. B* **557**, 237 (1999).
- [64] C. Gale, S. Jeon, and B. Schenke, *Int. J. Mod. Phys. A* **28**, 1340011 (2013).
- [65] B. Schenke, P. Tribedy, and R. Venugopalan, *Phys. Rev. C* **86**, 034908 (2012).
- [66] <https://github.com/schenke/ipglasma/>.
- [67] C. Adler *et al.* (STAR), *Phys. Rev. C* **66**, 034904 (2002).
- [68] B. Schenke, C. Shen, and P. Tribedy, *Phys. Lett. B* **803**, 135322 (2020).
- [69] H. Roch, N. Saß, and N. Götz, *smash-transport/sparkx: (v1.3.0)*, Zenodo 2024, <https://doi.org/10.5281/zenodo.12821236>.
- [70] M. Alvioli, H. J. Drescher, and M. Strikman, *Phys. Lett. B* **680**, 225 (2009).
- [71] G. K. Eyyubova, V. L. Korotkikh, A. M. Snigirev, and E. E. Zabrodin, *J. Phys. G: Nucl. Part. Phys.* **48**, 095101 (2021).
- [72] W. Broniowski, P. Bozek, and M. Rybczynski, *Phys. Rev. C* **76**, 054905 (2007).
- [73] F. G. Gardim, F. Grassi, M. Luzum, and J.-Y. Ollitrault, *Phys. Rev. C* **85**, 024908 (2012).
- [74] N. Borghini, M. Borrell, N. Feld, H. Roch, S. Schlichting, and C. Werthmann, *Phys. Rev. C* **107**, 034905 (2023).
- [75] A. Kurkela, A. Mazeliauskas, J.-F. Paquet, S. Schlichting, and D. Teaney, *Phys. Rev. C* **99**, 034910 (2019).
- [76] S. Schlichting, *PoS* **345**, 033 (2019).
- [77] U. W. Heinz and J. Liu, *Nucl. Phys. A* **956**, 549 (2016).
- [78] J. Liu, C. Shen, and U. Heinz, *Phys. Rev. C* **91**, 064906 (2015); **92**, 049904(E) (2015).
- [79] M. McNelis, D. Bazow, and U. Heinz, *Comput. Phys. Commun.* **267**, 108077 (2021).
- [80] D. Soeder, W. Ke, J. F. Paquet, and S. A. Bass, *arXiv:2306.08665*.
- [81] B. Schenke and S. Schlichting, *Phys. Rev. C* **94**, 044907 (2016).
- [82] L.-G. Pang, H. Petersen, G.-Y. Qin, V. Roy, and X.-N. Wang, *Eur. Phys. J. A* **52**, 97 (2016).
- [83] See Supplemental Material at <http://link.aps.org/supplemental/10.1103/PhysRevC.110.034901> for raw data of all figures.